Am J Transl Res 2025;17(12):9516-9530
www.ajtr.org /ISSN:1943-8141/AJTR0167534

Original Article

Ferroptosis-related genes and pathways in knee osteoarthritis cartilage degeneration: discovered by bioinformatics technology and in vivo experimental verification

Jun Dong[1,2,3*], Hui Su[4*], Tingting Zhou[2,3], Xiaoming Li[2,3], Hui Li[1]

[1]Department of Joint Surgery, Tianjin Medical University General Hospital, Tianjin 300052, China; [2]Department of Joint Surgery, Cangzhou Hospital of Integrated TCM-WM, Cangzhou 061001, Hebei, China; [3]Department of Joint Surgery, Hebei Key Laboratory of Integrated Traditional and Western Medicine in Osteoarthrosis Research, Cangzhou 061001, Hebei, China; [4]Department of Orthopedics, The First School of Clinical Medicine, Zhejiang Chinese Medical University, Hangzhou 310053, Zhejiang, China. [*]Equal contributors.

Received July 17, 2025; Accepted October 31, 2025; Epub December 15, 2025; Published December 30, 2025

Abstract: Objective: This study aimed to investigate the role of ferroptosis-related genes and pathways in cartilage degeneration in knee osteoarthritis (KOA) and to identify potential therapeutic targets. Methods: Integrated bioinformatics analysis of public KOA transcriptomic datasets was performed to identify differentially expressed ferroptosis-related genes. Key pathways and hub genes were further validated using a surgically-induced KOA mouse model and clinical cartilage samples through histology, immunohistochemistry, micro-CT, ELISA, western blot, and qPCR. Results: Significant iron deposition, mitochondrial damage, and dysregulation of ferroptosis markers (e.g., decreased GPX4 and increased p53) were observed in KOA cartilage. Key genes such as MMP2, SPP1, MYC, and BNIP3 were identified, and pathways including mTOR and HIF-1 signaling were enriched. Experimental results consistently indicated enhanced ferroptosis and matrix degradation in both mouse and human OA samples. Conclusion: Ferroptosis contributes significantly to KOA progression through iron overload, lipid peroxidation, and dysregulated metabolic pathways, providing new insight for targeted therapeutic strategies.

Keywords: Ferroptosis, osteoarthritis, bioinformatics, experimental, verification

Introduction

Osteoarthritis (OA) [1] is a common degenerative disorder characterized by the progressive deterioration of articular cartilage, inflammatory responses, and the formation of osteophytes at the bone margins [2]. With the aging global population, OA prevalence is on the rise, significantly impairing the quality of life for affected individuals. Although various treatment options, including pharmacological, physical, and surgical interventions, are available, they often merely alleviate symptoms rather than provide a cure [3]; therefore, it is vital to delve deeper into OA's pathogenesis and identify novel therapeutic targets. A newly discovered form of regulated cell death, has garnered considerable attention. Unlike traditional apoptosis and necrosis, ferroptosis is mainly triggered by the accumulation of lipid peroxides within cells, with iron ions playing a pivotal role in this process [4]. Research has demonstrated that ferroptosis contributes to the onset of various diseases, including neurodegenerative disorders, cardiovascular conditions, and certain cancers [5]. GPX4, a key regulator of ferroptosis, is significantly downregulated in the cartilage tissue of KOA patients, suggesting its protective role in OA development [6]. Other ferroptosis-related molecules, such as ACSL4 and FSP1, exhibit abnormal expression in the chondrocytes of OA patients, further underscoring the importance of ferroptosis in OA. Recent studies indicate that ferroptosis may significantly contribute to cartilage degeneration in OA, and by modulating specific gene expression

https://doi.org/10.62347/ZYBK5288

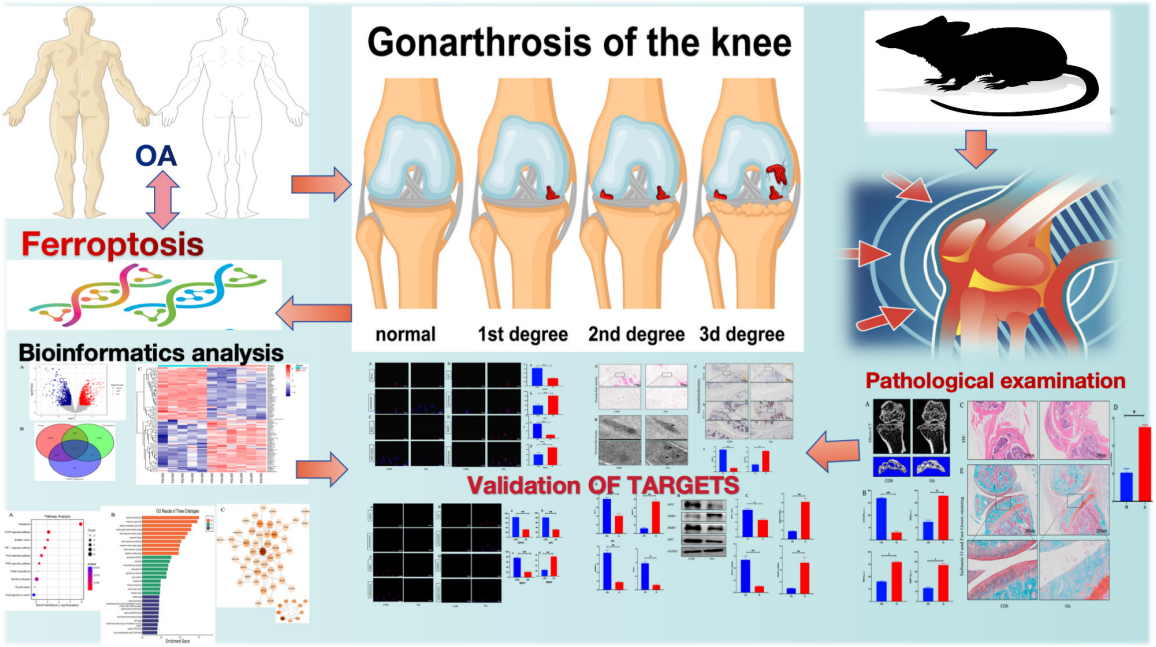

Figure 1. Graphical abstract.

or influencing related signaling pathways, ferroptosis can promote chondrocyte damage and inflammation, thereby accelerating KOA progression [7, 8]. Initial experimental research has demonstrated that blocking ferroptosis pathways can alleviate KOA symptoms. Utilizing iron chelators or antioxidants can reduce lipid peroxidation in chondrocytes, thus slowing down cartilage degeneration [9], laying a theoretical foundation for developing new therapeutic strategies targeting ferroptosis.

At present, the treatment of osteoarthritis mainly includes nonsteroidal anti-inflammatory drugs for analgesia and anti-inflammation, intravenous injection of glucocorticoids or hyaluronic acid to improve lubrication function, physical therapy, and end-stage joint replacement surgery, but these methods can only relieve symptoms rather than delay or reverse cartilage degeneration, and the efficacy is limited and long-term application may be accompanied by obvious side effects [10]. In recent years, studies based on bioinformatics technology have found that ferroptosis, a novel mode of cell death driven by iron-dependent lipid peroxidation, is closely related to OA cartilage degeneration. Previous studies have found abnormal expression of multiple ferroptosis-related genes (such as GPX4, ACSL4, SLC7A11, etc.) in OA cartilage tissue, suggesting that iron metabolism disorders, antioxidant defense mechanism failure, and lipid peroxidation accumulation may promote chondrocyte death and extracellular matrix degradation [11, 12]. A number of *in vivo* experiments [13, 14] confirmed that use of ferroptosis inhibitors can significantly reduce cartilage structure destruction and inflammatory responses in animal models, suggesting that targeting ferroptosis pathways may provide new strategies for OA treatment. Therefore, integrating bioinformatics screening and *in vivo* experimental validation, plus in-depth study of the role of ferroptosis-related genes and pathways in the process of OA will help us understand the mechanism and develop targeted therapy to delay cartilage degeneration. This research aims to conduct a thorough investigation into the roles and regulatory mechanisms of ferroptosis-associated genes and their networks during cartilage degeneration in OA. We will identify ferroptosis-related genes with differential expression, use bioinformatics methods to construct interaction networks among these genes, and pinpoint key regulatory nodes (**Figure 1**). Through exploring the ferroptosis pathway, we aim not only to unveil novel mechanisms underlying the pathogenesis of KOA but also to establish a

foundation for developing innovative therapeutic strategies for this condition.

Materials and methods

Bioinformatics techniques

Source of gene chip data: Gene expression data for OA cartilage tissue were extracted from the Gene Expression Omnibus (GEO) database (https://www.ncbi.nlm.nih.gov/geo/) using dataset GSE98918. The microarray platform employed was GPL20844 (Agilent-072363 SurePrint G3 Human GE v3 8x60K Microarray 039494). This dataset includes 12 OA samples (OA group) and 12 non-OA samples (normal control group). Using platform annotation files, "probe IDs" in the expression matrix were converted to "gene symbols". For genes associated with multiple probes, the average expression value was used to represent their expression levels.

Weighted Gene Co-expression Network Analysis (WGCNA): To build a co-expression network, the WGCNA package was employed, focusing on the top 25% most variably expressed genes from the GSE21942 dataset. The module exhibiting the strongest correlation with KOA was then pinpointed. Sample clustering was carried out to detect and eliminate outliers, while the optimal soft-thresholding power β was determined based on the scale-free topology criterion. Using this β value, adjacency was computed and subsequently converted into a topological overlap matrix (TOM). A hierarchical clustering tree was constructed based on the calculated β to demarcate gene modules. Principal component analysis (PCA) was performed on all genes within each co-expression module, and the first principal component, termed the module eigengene (ME), was identified. The Pearson correlation coefficient between ME values and the phenotype was calculated, and the module with the most robust correlation with MS was selected for further analysis.

Data processing and differential gene screening: Datasets pertaining to ferritin inhibitors, suppressors, and markers were sourced from the FerrDB database (http://www.zhounan.org/ferrdb) and then combined to identify genes linked to ferroptosis, and the common FR-DEGs in both tissues were identified. The GSE98918 dataset underwent preprocessing and normalization in R to obtain the probe expression matrix for each sample. DEGs were selected based on the criteria of $P < 0.05$, and $|\log_2$ fold change (log2FC)$| > 1$ was selected. Heatmaps were generated using the "pheatmap" package, while volcano plots were constructed utilizing the "ggplot2" package.

Gene Ontology (GO) and KEGG pathway analysis: The DAVID database was employed to conduct enrichment analysis of DEGs in GO terms and KEGG pathways. GO analysis served to elucidate the biological characteristics inherent in high-throughput genomic or transcriptomic data, whereas KEGG pathway analysis aimed to uncover signaling pathways linked to the DEGs. A significance threshold of $P < 0.05$ was set for gene enrichment, and the results were visually represented using the 'GOplot' package in R.

Protein-Protein Interaction (PPI) network analysis: Protein-Protein Interaction (PPI) network analysis was performed to identify pivotal functional associations among the differentially expressed genes (DEGs). The DEGs were imported into the STRING database (https://string-db.org/cgi/input.pl) to construct a preliminary interaction network with a confidence score threshold set at > 0.4. The resulting interaction data were then imported into Cytoscape software (version 3.7.2) for further topological analysis. Using the Degree algorithm in the cytoHubba plugin, key hub genes were systematically ranked based on their connectivity within the network. The top 10 candidate hub genes with the highest degree scores were selected as key targets, and a subnetwork centered around these genes was extracted and visualized to illustrate their direct and indirect interactions, thereby elucidating their potential central roles in the biological context.

Diagnostic performance analysis of marker genes: The efficacy of the marker genes for diagnosis was evaluated through receiver operating characteristic (ROC) curves and the area under the curve (AUC). ROC curve analysis was carried out using the pROC package in R, and the results were visualized with ggplot2.

In vivo experiments

Animal preparation: Eight- to ten-week-old male C57BL/6 mice, weighing 20-25 grams, were

randomly assigned to two groups: a control group (CON, n = 10) and an OA model group (n = 10). All mice were housed under standard conditions, with unrestricted access to food and water, at a temperature of 22-24°C and relative humidity of 50-60%. The animals were sourced from Henan SKB Biotech Co., LTD. (Animal Production License No. SCXK(Yu) 2020-0005) and accommodated in the Experimental Animal Center of Cangzhou Integrated Traditional Chinese and Western Medicine Hospital, Hebei Province, under natural lighting, with a maintained temperature of 20°C and relative humidity of 60%. This study received ethical approval from the Animal Ethics Committee of Cangzhou Integrated Traditional Chinese and Western Medicine Hospital (Review No. LL2023022203).

OA model construction: The OA model was created by surgical means. Mice were anesthetized using isoflurane: an initial 4-5% concentration for induction, then maintained at 1.5-2.5% in oxygen, administered through a precision vaporizer. Anesthesia depth was regularly checked to safeguard the animals during the procedure. Under sterile conditions, an incision was made over the knee joint skin, and the patella was shifted laterally to reveal the medial femoral condyle. With microsurgical tools, part of the meniscus was removed, and the medial collateral ligament was damaged, after which the skin was sutured. Control group mice underwent the same anesthesia and incision process but were spared meniscectomy or ligament injury [9]. After surgery, antibiotics were given daily for 7 days to ward off infection. The success of the OA modeling was evaluated at 8 weeks post-surgery through multiple methods: microscopic observation of articular cartilage structure using Safranin O/Fast Green staining confirmed proteoglycan loss and cartilage degradation; Osteoarthritis Research Society International (OARSI) scoring system was applied for semi-quantitative histological assessment, showing significantly higher scores in the DMM group compared to sham controls; micro-CT analysis revealed osteophyte formation and subchondral bone remodeling in operated joints; and immunohistochemical analysis indicated elevated expression of cartilage degeneration.

Sample collection: Following the completion of the experimental period, all mice were humanely euthanized. The euthanasia was performed by carbon dioxide (CO_2) asphyxiation in a gradually filled chamber, with a flow rate displacing 30% to 70% of the chamber volume per minute, followed by confirmation of death by cervical dislocation as a secondary physical method. This protocol is consistent with the recommendations of the AVMA Guidelines for the Euthanasia of Animals (2020) and was approved by the Institutional Animal Care and Use Committee (IACUC) to ensure minimal pain and distress was inflicted. After 8 weeks of gavage administration, right knee joint samples were harvested, and these samples were immediately fixed in 4% tissue fixative for 24 hours. Following thorough rinsing, they were immersed in a 70% ethanol solution and stored at 4°C for subsequent analysis.

Micro-CT scanning: The knee joints of the rats underwent scanning using a Micro-CT instrument (Skyscan1276) with the following optimized parameters: a voltage of 50 kV, a current of 200 μA, a full 360° rotation angle with a rotation increment of 0.4°, and a slice thickness of 9 μm. Post-scanning, the two-dimensional image sequences were automatically reconstructed into three-dimensional volumes with an isotropic voxel size of 15.9 μm, utilizing Skyscan NRecon software and the Feldkamp cone-beam algorithm. The trabecular bone microstructure and relevant parameters were analyzed using the Custom Analysis program (CTAn, Skyscan), which evaluated factors such as trabecular bone volume fraction, thickness, number, separation, and structure model index. Tomographic CT images were processed using CTAn and DataViewer software.

Biochemical detection by ELISA: The serum levels of COL2A1, MDA, SOD, and MMP-13 in the mice were quantified using ELISA kits, strictly adhering to the manufacturer's instructions. Absorbance readings for each well were taken at 450 nm using a microplate reader. Standard curves were constructed based on the correlation between concentration and absorbance values, enabling the calculation of the concentrations of the detected indicators in the samples.

Hematoxylin and Eosin (H&E) staining of articular cartilage: The samples were decalcified in a 14% EDTA solution for two weeks, thoroughly rinsed, and embedded in paraffin. The paraffin

sections were then dried on a slide warmer, and H&E staining was performed according to the kit instructions. After staining, the sections were dehydrated, cleared, and mounted with neutral gum for microscopic examination.

Safranin O-fast green staining of articular cartilage: The prepared cartilage paraffin blocks were cooled at 4°C for 20 minutes, and Safranin O-fast green staining was carried out following the kit's protocol. After staining, the sections were mounted with neutral gum and imaged under a microscope to observe articular cartilage changes.

Osteoarthritis Research Society International (OARSI) Scoring System: The severity of arthritis was assessed using the OARSI scoring system, and each sample was evaluated for cartilage structure, cellularity, matrix quality, and tidemark integrity, and scored according to OARSI grading and staging criteria. The OARSI score, calculated as the product of grade and stage, had a maximum possible value of 24 [12]. Higher scores indicated more severe cartilage degeneration.

Prussian blue staining: Paraffin sections of cartilage and subchondral bone were deparaffinized and rehydrated, and they were then stained with Prussian blue working solution for 60 minutes at room temperature. After removing the staining solution, the sections were washed three times with distilled water, and they were then stained with Prussian blue solution C for 3-5 minutes at room temperature, followed by rinsing in running tap water until colorless. The sections were dehydrated in absolute ethanol three times, each for 5 minutes, treated with xylene for 5 minutes, mounted with neutral gum, and examined under a microscope. Images were captured for further analysis.

Immunohistochemical staining: Sections were deparaffinized, rehydrated, and rinsed with distilled water. They were then incubated with 3% hydrogen peroxide at room temperature for 5 minutes, washed three times with PBS, and subjected to antigen retrieval in citrate buffer at 97.5°C for 10 minutes. After cooling to room temperature and washing with PBS, sections were blocked with 5% BSA at 37°C for 30 minutes. Primary antibodies against COL2A1 and SLC7A11 at a 1:100 ratio were applied, and sections were incubated overnight at 4°C. Following three PBS washes, sections were treated with a secondary antibody at 37°C for 30 minutes, washed again, and developed with DAB. After rinsing in tap water, sections were counterstained with hematoxylin for 30 seconds, differentiated with hydrochloric acid for 5 seconds, and blued in warm water for 3 minutes. Finally, sections were dehydrated, cleared in xylene, and mounted with neutral gum. Brown positive expression areas on the articular surface were observed and quantified using ImageJ software.

Transmission Electron Microscopy (TEM): Articular cartilage samples were thoroughly rinsed with physiological saline to remove debris. Observations were conducted under a transmission electron microscope at 80 kV, with a high vacuum environment maintained by extracting sufficient air from the sealed dark chamber. The microscopic structure of the cartilage surface was examined and photographed.

Immunofluorescence staining: Paraffin sections of joints were deparaffinized and rehydrated, followed by antigen retrieval with citrate buffer. Endogenous peroxidase activity was neutralized with 3% H_2O_2, and sections were permeabilized with 1% Triton X-100 for 30 minutes and blocked with 5% BSA for another 30 minutes. Primary antibodies against GPX4, p53, SPP1, and MMP-2 (diluted 1:300) were applied, and sections were incubated overnight at 4°C. After three PBS washes, sections were incubated with a FITC-conjugated secondary antibody (diluted 1:300) in the dark at room temperature for one hour. Following another three PBS washes, sections were stained with DAPI for 10 minutes and examined for target marker expression.

Clinical cartilage sample collection: Clinical cartilage samples were collected from patients undergoing total knee arthroplasty (TKA) for advanced knee osteoarthritis (OA) (n = 4, 2 male and 2 female). Normal control cartilage samples were obtained from patients receiving lower limb amputation due to non-OA causes such as trauma or vascular disease (n = 4, 2 male and 2 female). Based on the International Cartilage Repair Society (ICRS) grading system, OA samples were classified as damaged (ICRS grades 1-4), while control samples were

Table 1. List of PCR primer sequences

	Forward	Reverse
COL2A1	5'-GAGAGCAACAGGCTGGTAT-3'	5'-TGTGTTTCCAGGTTTCCAG-3'
GPX4	5'-TGCAGGAGGAGAAGGAGAA-3'	5'-GCTGAGGAGGAAGGAGTAG-3'
SLC7A11	5'-TCTGCGGAGGAGGAGGAG-3'	5'-TCCTGAGGAGGAGGAGGAG-3'
p53	5'-TGAGGAGGAGGAGGAGGAG-3'	5'-TCTGAGGAGGAGGAGGAGG-3'
MMP13	5'-TGGAGGAGGAGGAGGAG-3'	5'-TCTGAGGAGGAGGAGGAG-3'
MYC	5'-TCTGAGGAGGAGGAGGAG-3'	5'-TCTGAGGAGGAGGAGGAG-3'

confirmed as undamaged (ICRS grade 0) [15]. Inclusion criteria for the OA group included: diagnosis of primary knee OA according to ACR criteria, age between 60-80 years, and undergoing primary TKA. Controls were included based on: absence of history of joint disease, normal radiographic appearance of the knee, and ICRS grade 0 confirmed macroscopically and histologically. Exclusion criteria for both groups comprised: inflammatory arthritis (e.g., rheumatoid arthritis), previous knee surgery, infectious arthropathy, chondrocalcinosis, and significant medical comorbidities affecting cartilage metabolism. The study was approved by the Ethics Committee of Cangzhou Integrated Traditional Chinese and Western Medicine Hospital, Hebei Province (IRB: CZX2023-KY-152.1). All participants provided written informed consent prior to participation, in compliance with the World Medical Association's Helsinki Declaration and relevant ethical requirements.

Western blot: Cartilage tissues from each group were homogenized and lysed, and protein concentrations were measured using the BCA method. Proteins were separated by electrophoresis, transferred to membranes, and blocked at room temperature for 2 hours. The membranes were then incubated overnight at 4°C with the following primary antibodies: Anti-Collagen II (Abcam 34712, 1:1000), Anti-Glutathione Peroxidase 4 (GPX4) (Abcam 125066, 1:1000), Anti-SLC7A11 (Abcam 307601, 1:1000), p53 (Abcam PAb 240, 1:1000), MMP13 (Abcam 219620, 1:1000), MYC (Abcam 185656, 1:1000), SPP1 (Abcam 283656, 1:1000), MMP2 (Abcam 92536, 1:1000), BNIP3 (Abcam 109362, 1:1000), and β-actin (Abcam 8226, 1:1000). After thorough washing, the membranes were incubated with horseradish peroxidase (HRP)-conjugated secondary antibodies (diluted 1:5000) at room temperature for 2 hours. Blots were developed using a chemiluminescent substrate, and band intensities were analyzed with ImageJ software.

Real-time PCR: Real-time quantitative polymerase chain reaction (qPCR) was performed to measure the mRNA expression levels of target genes. Total RNA was extracted from cartilage tissues or cells using TRIzol reagent, and its concentration and purity were assessed spectrophotometrically. cDNA was synthesized from 1 μg of total RNA using a PrimeScript™ RT reagent kit with gDNA Eraser according to the manufacturer's protocol. The qPCR reaction was carried out in a 20 μL system containing 2 μL of cDNA template, 10 μL of TB Green® Premix Ex Taq™, 0.8 μL of each forward and reverse primer (10 μM), and 6.4 μL of RNase-free water. The amplification conditions consisted of an initial denaturation at 95°C for 30 seconds, followed by 40 cycles of 95°C for 5 seconds and 60°C for 30 seconds. Each sample was run in triplicate, and a no-template control was included in each run to monitor potential contamination. The relative expression of genes was calculated using the $2^{-\Delta\Delta Ct}$ method, with GAPDH serving as the internal reference gene for normalization. The primer sequences used in the PCR experiment are shown in **Table 1**.

Statistical analysis

All statistical analyses were performed using SPSS software (version 26.0). Continuous variables that followed a normal distribution are expressed as mean ± standard deviation. For multi-group comparisons of normally distributed data with homogeneity of variance, one-way analysis of variance (ANOVA) was applied, and post-hoc pairwise comparisons were conducted using the least significant difference (LSD) test. In cases where variances were unequal, Welch's ANOVA was used for multi-group comparisons, followed by the Kruskal-Wallis H test

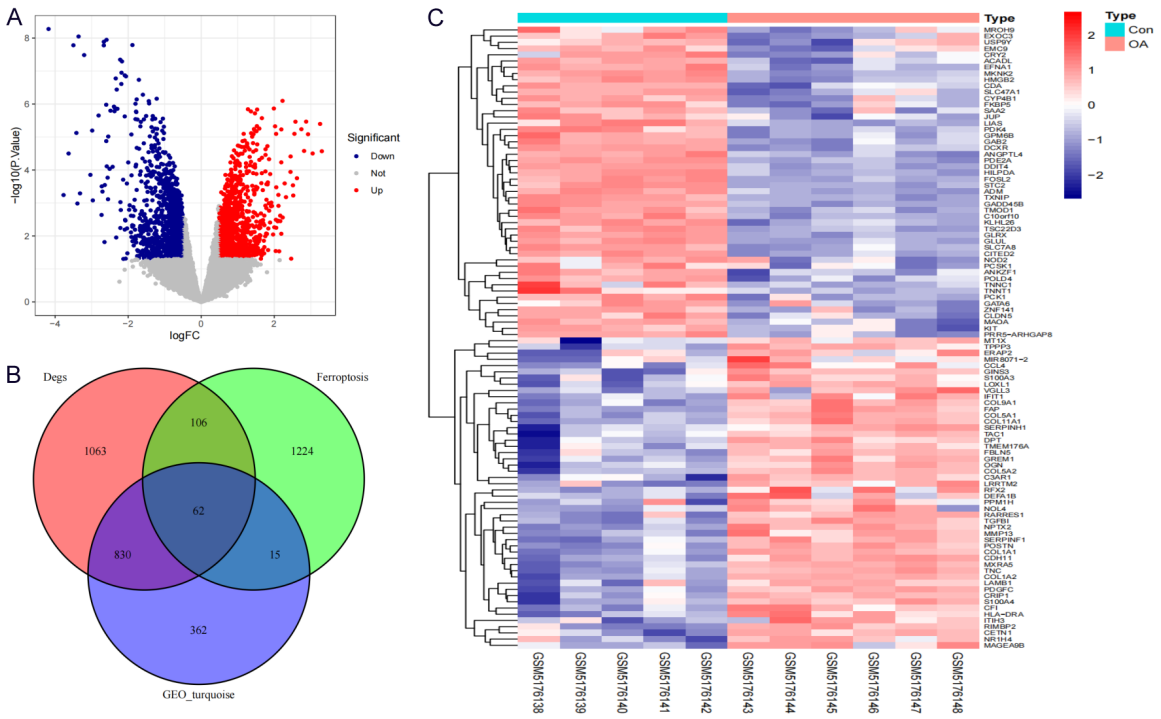

Figure 2. Integrative Analysis of Differential Gene Expression and Ferroptosis in Osteoarthritis. A. Volcano plot illustrating significant differentially expressed genes (DEGs) in canine samples, highlighting upregulated (red) and downregulated (blue) genes relative to control samples. B. Venn diagram depicting the overlap of DEGs associated with ferroptosis and other identified pathways in canine osteoarthritis. C. Heatmap displaying the expression levels of significant DEGs across various samples, with hierarchical clustering to reveal patterns of expression between control (Con) and osteoarthritis (OA) groups. The color scale indicates normalized expression values, ranging from downregulation (blue) to upregulation (red).

for subsequent pairwise analysis. The Kruskal-Wallis H test was also employed for comparing categorical data across groups. A two-sided *P*-value of less than 0.05 was considered significant for all tests.

Results

Bioinformatics analysis identifying ferroptosis-related target genes and pathways in OA

The volcano plot illustrates the relationship between gene expression significance and fold change (**Figure 2A**, **2B**). The heatmap reveals marked upregulation or downregulation of multiple genes in the OA group (**Figure 2C**), indicating significant differences in ferroptosis-related gene expression between arthritic and normal cartilage. The analysis identified 62 ferroptosis-associated genes, highlighting their strong correlation and potential pivotal role in arthritis pathogenesis. Using WGCNA, we discovered 20 gene modules linked to ferroptosis and arthritis. Correlation analysis showed a significant positive association between the MEblue module and ferroptosis characteristics ($r = 0.76$, $P < 0.001$), while arthritis severity was negatively correlated with the MEred module ($r = -0.65$, $P < 0.01$) (**Figure 3A**). The gene dendrogram (**Figure 3B**) supports the differentiation of these modules (**Figure 3C**), with the dynamic tree cut method effectively partitioning distinct modules. Scale independence analysis indicated that, at a soft threshold power of 6, the network exhibits high scale-free characteristics, with highly connected modules (mean > 500) primarily associated with ferroptosis-related features (**Figure 3D**). These findings underscore the potential role of specific gene modules in the pathological mechanisms of ferroptosis and arthritis, laying the groundwork for future therapeutic targets.

Bioinformatics analysis also identified key signaling pathways and interactions associated with ferroptosis and arthritis-related genes. Pathway analysis revealed the ferroptosis pathway as the most significantly enriched (**Figure 4A**), with an enrichment score of 5.5 ($P < 0.005$), followed by the mTOR and HIF-1 signal-

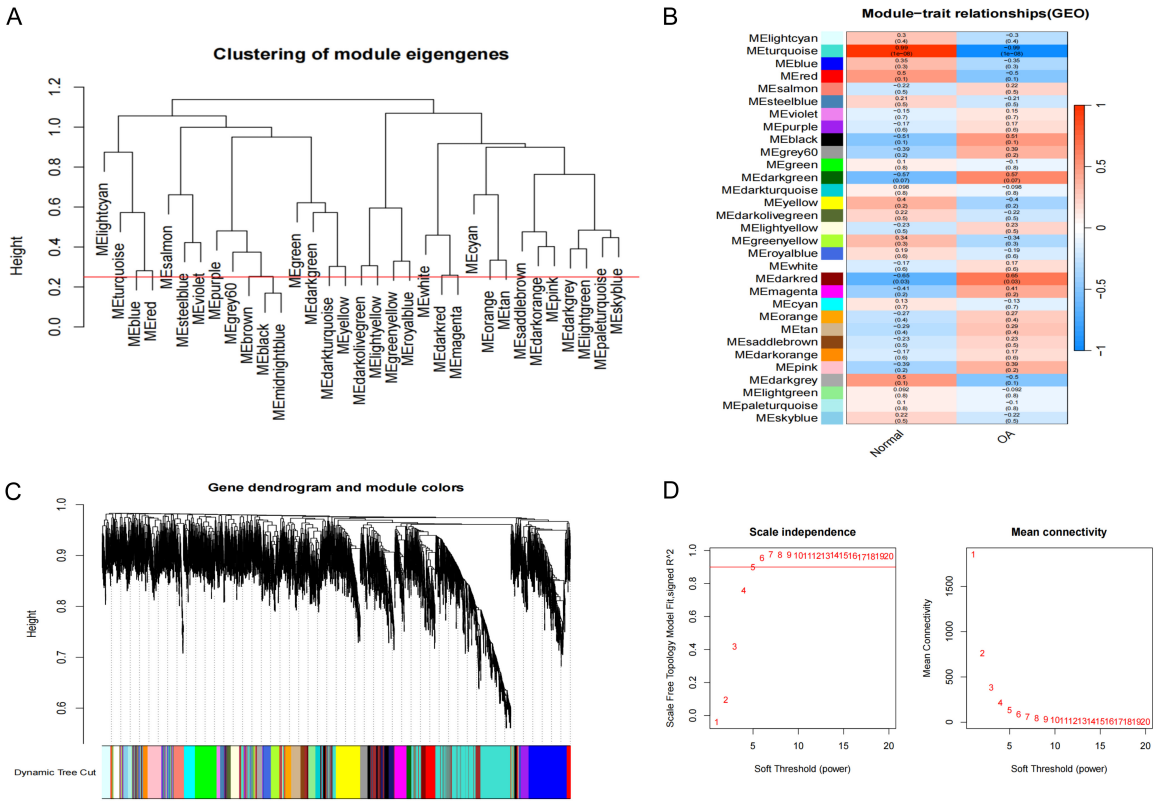

Figure 3. Analysis of Module Eigengene Clustering and Trait Relationships in Gene Expression Data. (A) The hierarchical clustering of module eigengenes, highlighting distinct clustering patterns. (B) The correlation matrix of module-trait relationships, indicating significant associations between specific modules and traits. (C) Panel features a gene dendrogram alongside module colors. Finally, (D) scale independence and mean connectivity through various soft threshold powers, essential for validating network topology.

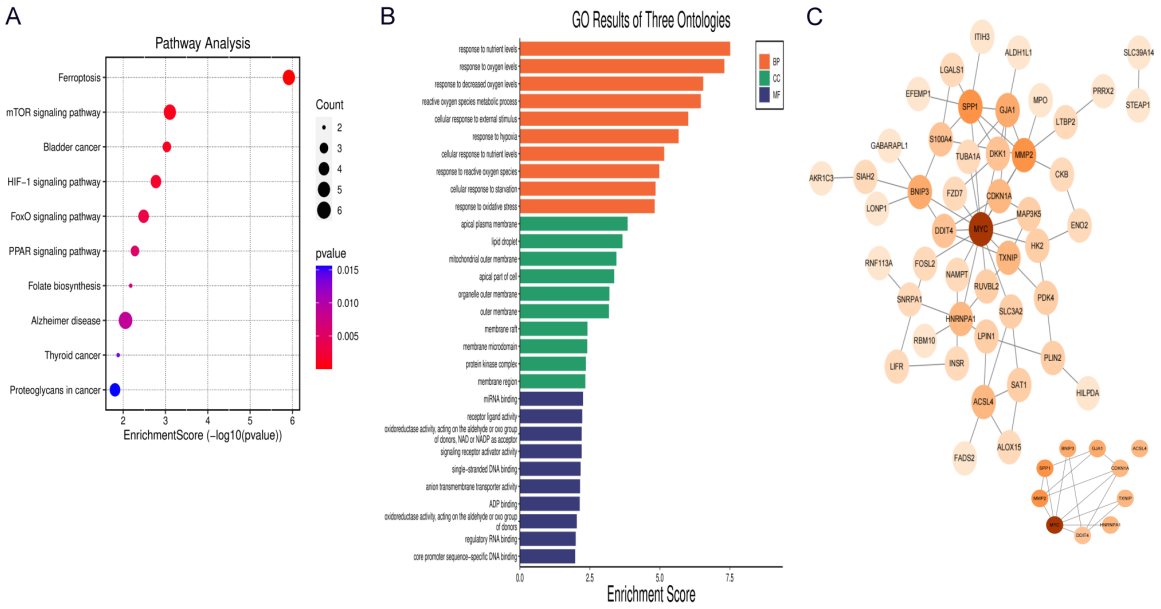

Figure 4. Pathway and Gene Ontology Analysis Reveals Key Biological Processes and Pathways Associated with Disease Mechanisms. A. Pathway analysis illustrating the enrichment scores and significance of various pathways, including the mTOR signaling pathway and Alzheimer's disease, represented by bubble size and color coding based on *p*-values. B. Gene Ontology (GO) results for three ontologies, highlighting the enrichment scores of biological

processes, cellular components, and molecular functions. C. Network visualization of significant genes associated with the identified pathways and GO terms, showing interactions and relationships among key regulatory elements.

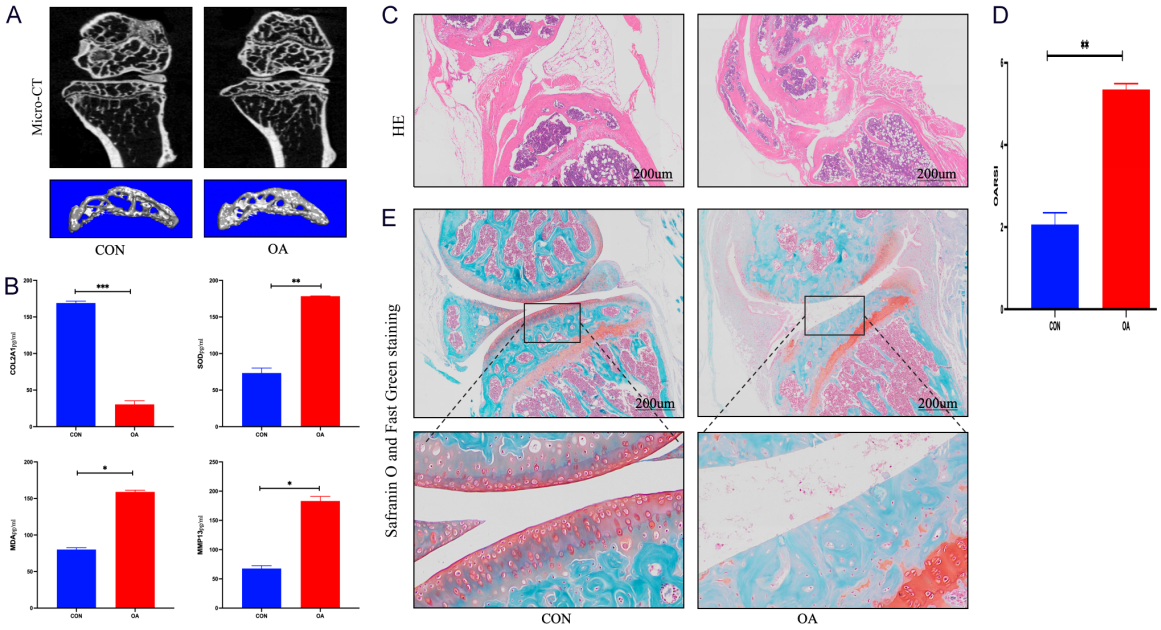

Figure 5. Pathologic examination of bone microstructure. A. Micro-CT scanning and analysis of the knee joint of mice. B. ELISA for serum Col2a1, SOD, MDA and MMP13 in each group. C. Histological staining (scale bar = 200 μm). D. Safranin O and Fast Green staining staining (scale bar = 200 μm). E. OARSI score. Values are expressed as mean ± SD, n = 10; *P < 0.05, **P < 0.01, ***P < 0.001, ****P < 0.0001.

ing pathways (P < 0.01). Pathways related to bladder cancer, PPAR signaling, Alzheimer's disease, and thyroid cancer were also identified, suggesting potential links between these conditions and ferroptosis. GO analysis highlighted enriched biological processes such as response to oxidative stress and reactive oxygen species, emphasizing the role of oxidative stress in the pathogenesis of both ferroptosis and arthritis (**Figure 4B**). The PPI network underscored the importance of the hub gene VGC (Vascular Growth Factor) (**Figure 4C**), which connects various pathways and biological processes. Key interacting genes, including ITM2A, ALDH1A1, and MPO, emerged as critical players, suggesting their potential as therapeutic targets. Using the Maximal Clique Centrality (MCC) algorithm, we identified pivotal genes such as MYC, MMP2, SPP1, BNIP3, GJA1, CDKA1N, and TXNIP, and illustrated their interactions with other differentially expressed ferroptosis-related genes (DEFRGs) (**Figure 4C**).

Our findings suggest that ferroptosis-linked genes may significantly impact OA development. Integrating differential expression analysis and gene overlap assessments provides insight into the potential mechanisms linking iron metabolism and joint inflammation, warranting further investigation into therapeutic targets for OA management.

Pathologic and biochemical manifestations of cartilage degeneration and ferroptosis in OA mice

Micro-CT analysis of subchondral bone (**Figure 5A**) revealed that the CON group exhibited an orderly trabecular arrangement with appropriate thickness and spacing. In contrast, the OA model group demonstrated a significant increase in subchondral bone volume, characterized by reduced trabecular spacing and severe sclerosis. Serum ELISA assays (**Figure 5B**) demonstrated a marked reduction in the cartilage-specific collagen factor Col2a1 in the OA group compared to the control, alongside significant increases in ferroptosis-related oxidative stress markers SOD and MDA, as well as the inflammatory factor MMP13 (P < 0.001). Histologic examination using HE stain-

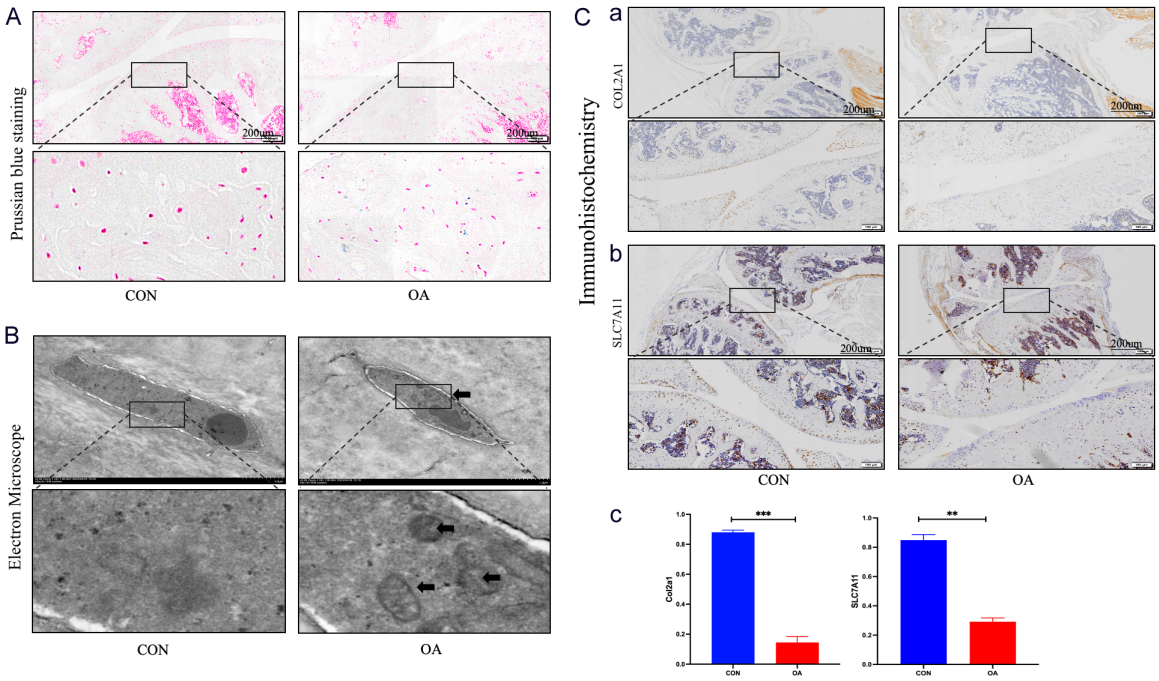

Figure 6. Ferroptosis related pathological examination of knee joint. (A) Prussian blue staining of mice in each group. (B) The electron microscope of microstructure. (C) Immunohistochemistry of femoral tissue of (a) Col2al, (b) SLC7A11 (active cell stained in brown, scale bar = 200 μm). (c) Immunohistochemical statistical bar graph, Values are expressed as mean ± SD, n = 10; *P < 0.05, **P < 0.01, ***P < 0.001, ****P < 0.0001.

ing (**Figure 5C**) showed normal cartilage morphology in the CON group, with a smooth, continuous surface and no significant meniscal damage or pathologic changes. Conversely, the OA group exhibited a rough, discontinuous articular cartilage surface with fissures extending into the subchondral layer and meniscal pathology. OARSI pathological scoring revealed significantly increased cartilage degeneration in OA mice (P < 0.001) (**Figure 5D**). Safranin O-fast green staining (**Figure 5E**) further confirmed distinct pathologic changes in the OA group, including cartilage wear and fissuring, with significant differences from the control (P < 0.001).

Prussian blue staining, which highlights trivalent iron ions, revealed significant iron particle deposits stained deep blue in the knee joint cartilage of the OA group compared to the control (**Figure 6A**), suggesting marked iron overload associated with cartilage degeneration in OA. Electron microscopy examination of mitochondrial morphology and density in cartilage tissue showed that, compared to the CON group, the OA group exhibited reduced or absent mitochondrial cristae, increased membrane density, and cytoplasmic vacuoles - characteristic pathological alterations indicative of ferroptosis (**Figure 6B**). Immunohistochemical analysis corroborated the activation of ferroptosis targets in the OA model. The positive expression of the cartilage-specific factor Col2a1 was significantly reduced in the articular cartilage of OA mice compared to the CON group, as was the expression of the ferroptosis negative regulator SLC7A11 (**Figure 6Ca**, **6Cb**), with statistically significant differences (P < 0.001) (**Figure 6Cc**). Immunofluorescence analysis of mouse knee joints (**Figure 7**) further demonstrated significant differences in the expression of cartilage and ferroptosis-related targets between the CON and OA groups. Specifically, GPX4 expression was significantly diminished in the OA group (**Figure 7A**, **7Aa**), indicating reduced antioxidant capacity of chondrocytes under osteoarthritic conditions. Conversely, the ferroptosis positive regulator p53 was significantly elevated in the OA group (P < 0.001) (**Figure 7B**, **7Bb**). Additionally, SPP1 and MMP2 expression levels showed an upward trend in the OA group (P < 0.001)

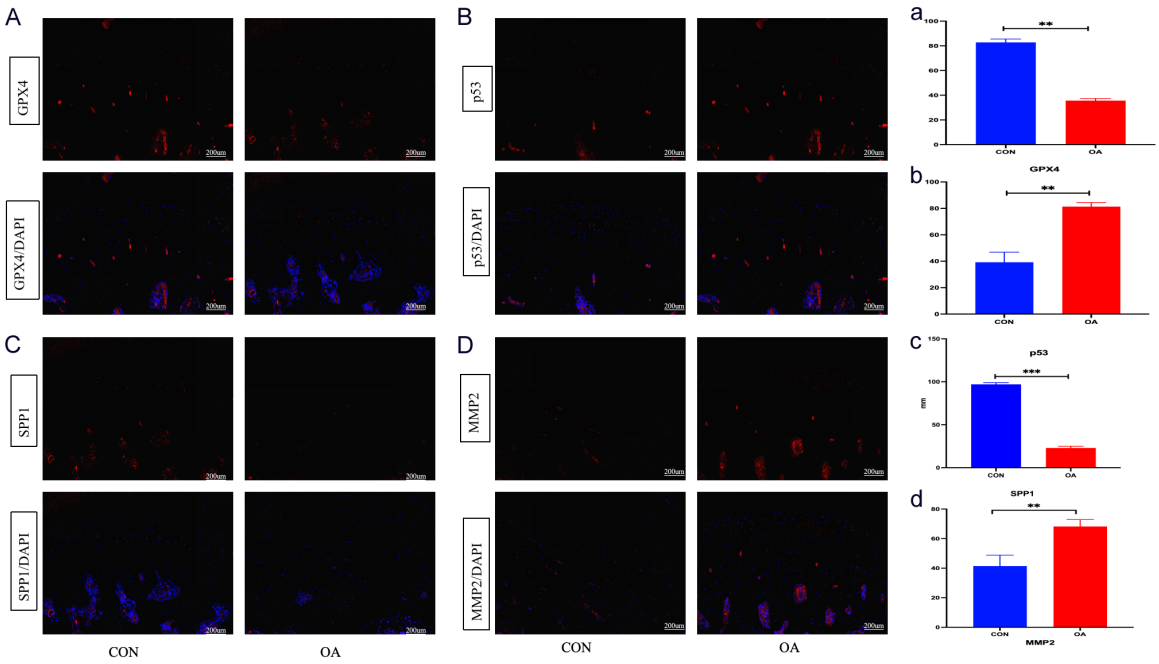

Figure 7. Immunofluorescence staining of cartilage tissue of mouse knee joint, Images are arranged in a grid format, with scale bars indicating 200 μm. (A) GPX4, (B) P53, (C) SPP1, (D) MMP2; (a-d) Corresponding quantitative analysis of Immunofluorescence staining. Values are presented as mean ± SD, n = 10; *P < 0.05, **P < 0.01, ***P < 0.001, ****P < 0.0001.

(**Figure 7C**, **7D**, **7Cc**, **7Dd**), further indicating cartilage tissue damage and remodeling processes. Overall, these findings suggest that changes in the expression of cartilage and ferroptosis-related targets in the OA group may be closely linked to the pathologic progression of arthritis.

Co-expression of cartilage and ferroptosis-related targets in clinical cartilage samples demonstrates a clear association

Immunofluorescence analysis of clinical cartilage samples (**Figure 7**) revealed a notable decrease in the cartilage growth factor COL2A1 in the OA group compared to the CON group (**Figure 7A**, **7Aa**), while the expression of the cartilage-degrading matrix metalloproteinase MMP13 was significantly elevated. Among ferroptosis-related factors, the OA group exhibited marked suppression of the negative regulators GPX4 and SLC7A11, alongside a significant increase in the positive regulator P53 compared to the CON group (**Figure 7B**, **7Bb**), with statistical significance ($P < 0.001$). Furthermore, SPP1 and MMP2 expression levels were significantly lower in the OA group (**Figure 7C**, **7D**, **7Cc**, **7Dd**), also achieving significance ($P < 0.001$). These findings indicate exacerbated cartilage matrix degradation and enhanced inflammatory responses in OA. Protein and RNA analyses were conducted on clinically obtained cartilage samples. Western blotting and quantitative PCR (QT-PCR) revealed that (**Figure 8**), compared to the CON group, the OA group exhibited significant downregulation of Col2a1, GPX4, and SLC7A11 proteins (**Figure 8A**, **8B**), as well as their total RNA expression. Conversely, P53 and MMP13 proteins and total RNA (**Figure 8C**) were significantly upregulated in the OA group (all $P < 0.001$).Based on previous bioinformatics findings, we performed experimental analyses, including reverse transcription polymerase chain reaction and western blot. These analyses revealed significant differences in targeted protein expression between the CON and OA groups (**Figure 9**). Specifically, MYC protein and its mRNA levels were significantly higher in the CON group than in the OA group ($P < 0.01$), suggesting a more critical role for MYC in the control group. Conversely, MMP2 protein and mRNA expression were significantly elevated in the OA group relative to the CON group ($P < 0.001$), indicating a potential link between MMP2 and OA pathological progression (**Figure 9A**, **9B**). BNIP3 pro-

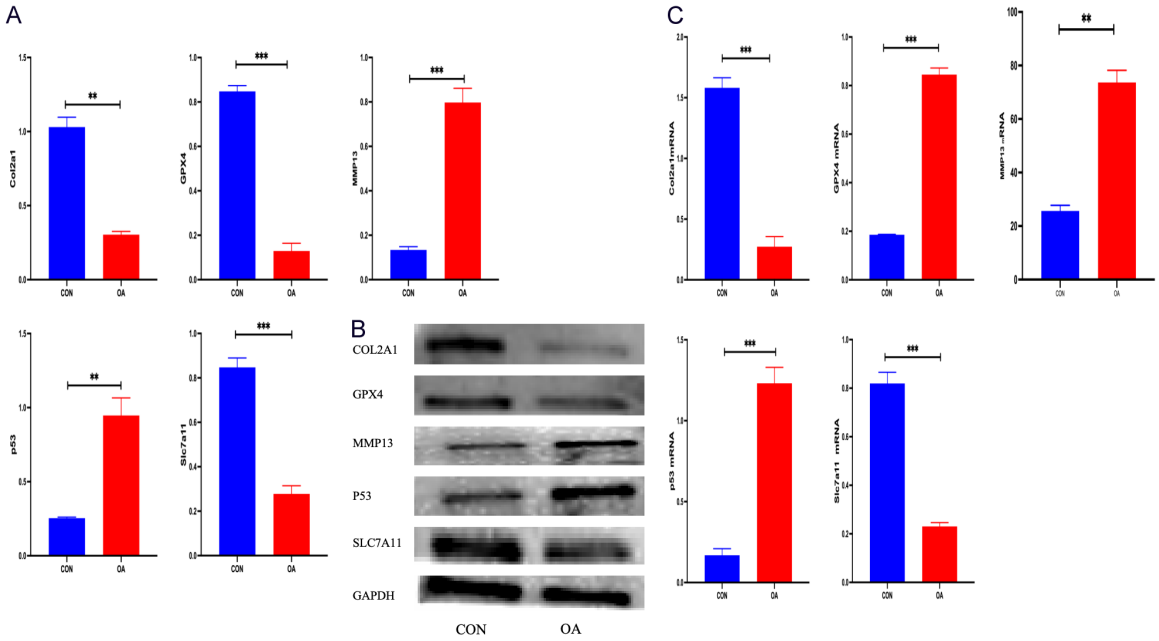

Figure 8. Expression of Ferroptosis and cartilage related factor in cartilage tissue of knee joint of mice in each group. A. Gray value statistics from western blot for each group. B. Western blot bands in grayscale. C. Statistics of gray value histograms for QT PCR in each group, Values are expressed as mean ± SD, n = 10; *P < 0.05, **P < 0.01, ***P < 0.001, ****P < 0.0001.

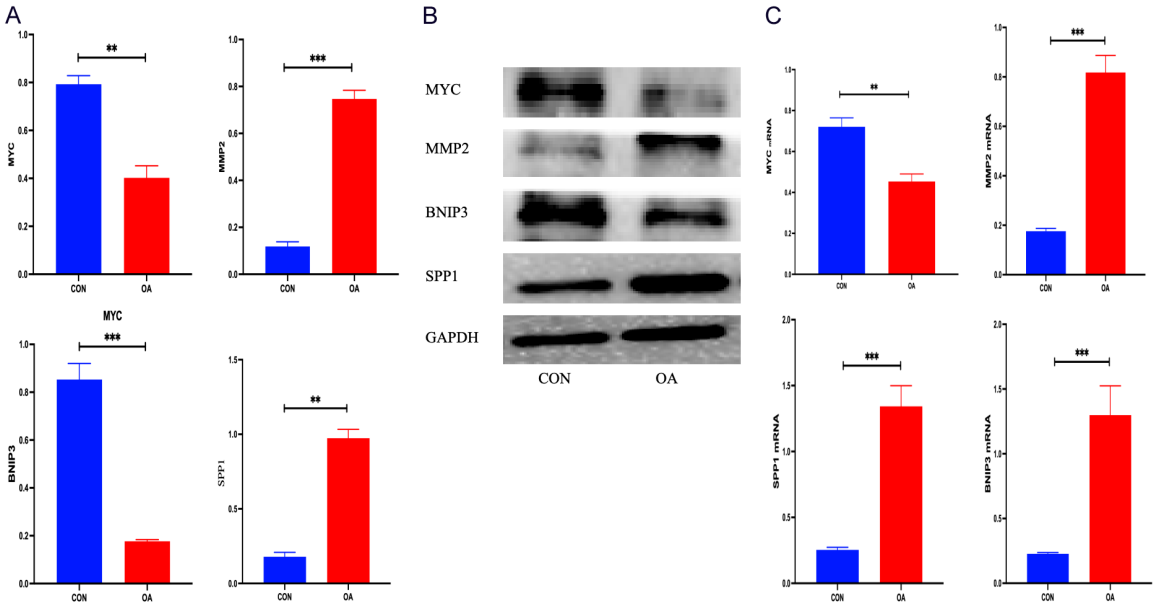

Figure 9. Expression of Ferroptosis and cartilage related factor in collected human cartilage tissue. A. Gray value statistics from western blot for each group. B. Western blot bands in grayscale. C. Histogram statistics of gray values for QT PCR in each group. Values are expressed as mean ± SD, n = 10; *P < 0.05, **P < 0.01, ***P < 0.001, ****P < 0.0001.

tein and mRNA were significantly more abundant in the CON group than in the OA group (P < 0.001), whereas SPP1 protein and mRNA expression were significantly greater in the OA group compared to the CON group (P < 0.01) (**Figure 9C**), and these results highlight sub-

stantial differences in the expression levels of MYC, BNIP3, MMP2, and SPP1 between the CON and OA groups, possibly reflecting distinct biological functions and underlying pathological mechanisms in each group.

Discussion

Recent studies have underscored the significant link between ferroptosis and knee joint diseases, including OA, rheumatoid arthritis, and other joint disorders [14]. Iron, vital for cellular function, can induce oxidative stress and cellular damage when in excess [16]. Abnormal iron accumulation in joint tissues is closely associated with inflammatory responses and cell death [17]. In knee joint diseases, iron overload may worsen chondrocyte damage, promote inflammation, and hasten joint degeneration. Studies indicate a notable relationship between iron overload in OA patients' articular cartilage and the onset of ferroptosis [13], which may lead to chondrocyte death, affecting cartilage structure and function. Our findings demonstrate a significant association between ferroptosis and the pathogenesis of OA, which is supported by both *in vivo* mouse model data and clinical sample analyses. The observed pathological changes - including mitochondrial shrinkage, increased membrane density, iron deposition, and dysregulation of ferroptosis-related markers such as GPX4 and p53 - are consistent with previously established hallmarks of ferroptosis reported in studies focusing on metabolic and degenerative disorders [18, 19]. Notably, the upregulation of MMP2 and SPP1 in OA cartilage aligns with findings [20], who also described their roles in extracellular matrix degradation and inflammation. Similarly, the central role of genes such as MYC and BNIP3 in modulating oxidative stress and mitophagy corroborates earlier work in cancer and neurodegeneration [15, 21], though their involvement in chondrocyte ferroptosis introduces a novel dimension to OA pathophysiology. The enrichment of mTOR and HIF-1 signaling pathways further supports the interplay between metabolic reprogramming and ferroptosis, as recently highlighted in studies on age-related joint degeneration. However, some of our results, such as the downregulation of MYC in OA tissues, appear to contradict its previously reported pro-ferroptotic role in cancer models, suggesting cell- and context-specific functions that warrant further investigation.

Although we made these insights, this study still has some limitations. The sample size, especially that of the clinical group, was relatively small, which may affect the general applicability of the research results. Additionally, although we identified multiple genes and pathways related to ferroptosis through bioinformatics and experimental verification, the precise mechanism connection between iron metabolism imbalance, mitochondrial dysfunction and cartilage degeneration is still not fully clear. A deeper understanding of the specific mechanism of ferroptosis in osteoarthritis may lead to the discovery of new therapeutic targets and strategies for the early diagnosis, prevention and treatment of this disease. The research conducted a systematic exploration of the impact and regulatory networks of ferroptosis-associated genes in the degeneration of knee osteoarthritis (KOA) cartilage. By integrating comprehensive bioinformatics analyses with *in vitro* and *in vivo* experiments, our results suggest that ferroptosis may drive the progression of KOA by influencing iron metabolism, oxidative stress responses, and cartilage matrix degradation. We identified key ferroptosis-related genes, including MYC, MMP2, SPP1, and BNIP3, as potential therapeutic targets, and highlighted the involvement of oxidative stress and hypoxia signaling pathways. The functional effects of these genes and pathways were validated through both animal and clinical sample experiments. These findings not only enhance our understanding of the pathogenic mechanisms underlying KOA but also provide a foundation for the development of novel treatment strategies, ultimately improving the quality of life for KOA patients.

Acknowledgements

This project was sponsored by the Foundation of Health Commission of Hebei Province (20241622); Scientific Research Program of Hebei Provincial Administration of Traditional Chinese Medicine (2024477).

Disclosure of conflict of interest

None.

Address correspondence to: Xiaoming Li, Department of Joint Surgery, Cangzhou Hospital of Inte-

grated TCM-WM, 31 Huanghe Road, Cangzhou 061000, Hebei, China. E-mail: lixiaomingcz@126.com; Hui Li, Department of Joint Surgery, Tianjin Medical University General Hospital, 154 Anshan Road, Heping District, Tianjin 300052, China. E-mail: sh130921@163.com

References

[1] de Roy L, Teixeira GQ, Schwer J, Sukopp M, Faschingbauer M, Ignatius A and Seitz AM. Structure-function of cartilage in osteoarthritis: an ex-vivo correlation analysis between its structural, viscoelastic and frictional properties. Acta Biomater 2024; 190: 293-302.

[2] Wang J, Yang J, Fang Y, Lou C, Yu H, Li Y, Lv J, Chen H, Cai L and Zheng W. Vinpocetine protects against osteoarthritis by inhibiting ferroptosis and extracellular matrix degradation via activation of the Nrf2/GPX4 pathway. Phytomedicine 2024; 135: 156115.

[3] Zhao C, Kong K, Liu P, Chen X, Rong K, Zhang P, Wang L and Wang X. Regulating obesity-induced osteoarthritis by targeting p53-FOXO3, osteoclast ferroptosis, and mesenchymal stem cell adipogenesis. Nat Commun 2025; 16: 4532.

[4] Zou Z, Hu W, Kang F, Xu Z, Li Y, Zhang J, Li J, Zhang Y and Dong S. Interplay between lipid dysregulation and ferroptosis in chondrocytes and the targeted therapy effect of metformin on osteoarthritis. J Adv Res 2025; 69: 515-529.

[5] Zhang Y, Li J, Liu J, Gao Y, Li K, Zhao X, Liu Y, Wang D, Hu X and Wang Z. Ferroptosis in osteoarthritis: towards novel therapeutic strategy. Cell Prolif 2025; 58: e13779.

[6] Gao ZY, Yan GQ, Su L, He SS, Sheng JE, Wu QC, Huang X and Dai YF. Transcriptomic analysis and experimental verification of ferroptosis signature genes in osteoarthritis. Int J Rheum Dis 2025; 28: e70083.

[7] Yu B, Zeng A, Liu H, Yang Z, Gu C, Luo X and Fu M. LncRNA HOXA11-AS intercepts the POU2F2-mediated downregulation of SLC3A2 in osteoarthritis to suppress ferroptosis. Cell Signal 2024; 124: 111399.

[8] Yue Y, Wei Y, Sheng W, Cao S, Li Y, Li A, Yu F, Weng J, Li W, Xiong A, Wang D, Zeng H, Lin J and Liu P. Multifunctional biomimetic nanomedicine for osteoarthritis alleviation by mitigating cartilage degeneration and promoting cartilage regeneration. ACS Appl Mater Interfaces 2025; 17: 40288-40302.

[9] Zhuang H, Ren X, Li H, Zhang Y and Zhou P. Cartilage-targeting peptide-modified cerium oxide nanoparticles alleviate oxidative stress and cartilage damage in osteoarthritis. J Nanobiotechnology 2024; 22: 784.

[10] Zhao Z, Wang P, Li Z, Wei X, Li S, Lu X, Dai S, Huang B, Man Z and Li W. Targeted lipid nanoparticles distributed in hydrogel treat osteoarthritis by modulating cholesterol metabolism and promoting endogenous cartilage regeneration. J Nanobiotechnology 2024; 22: 786.

[11] Wan J, Shen F, Ding J and Ye D. ZEB1 silencing protects against ferroptosis and mitochondrial dysfunction in osteoarthritis by inhibiting HSPA5 expression. Immunopharmacol Immunotoxicol 2025; 47: 563-576.

[12] Wang D, Pan Y, Chen W, He D, Qi W, Chen J, Yuan W, Yang Y, Chen D, Wang P and Jin H. Nanodrugs targeting key factors of ferroptosis regulation for enhanced treatment of osteoarthritis. Adv Sci (Weinh) 2025; 12: e2412817.

[13] He X, Tian K, Lin X, Chen X, Su Y, Lu Z, Chen Z, Zhang L, Li P, Ma L, Feng G, Zhao X, Lan Z, Zhang C, Xue D and Jin Q. Unveiling the role of RhoA and ferroptosis in vascular permeability: implications for osteoarthritis. Int J Mol Med 2024; 54: 86.

[14] Hiruthyaswamy SP, Bose A, Upadhyay A, Raha T, Bhattacharjee S, Singha I, Ray S, Nicky Macarius NM, Viswanathan P and Deepankumar K. Molecular signaling pathways in osteoarthritis and biomaterials for cartilage regeneration: a review. Bioengineered 2025; 16: 2501880.

[15] Sun Q, Zhang Y, Hu B, Feng Q, Xia Y, Yu L, Zhang C, Liu W, Liu Z, Yao H and Lang Y. Development of a dual-responsive injectable GelMA/F127DA hydrogel for enhanced cartilage regeneration in osteoarthritis: harnessing MMP-triggered and mechanical stress-induced release of therapeutic agents. Int J Biol Macromol 2025; 304: 140823.

[16] Hao X, Zhao J, Jia L, Ding G, Liang X, Su F, Yang S, Yang Y, Fan J, Zhang WJ, Yang L and Jie Q. LATS1-modulated ZBTB20 perturbing cartilage matrix homeostasis contributes to early-stage osteoarthritis. Bone Res 2025; 13: 33.

[17] He X, He S, Xiang G, Deng L, Zhang H, Wang Y, Li J and Lu H. Precise lubrication and protection of cartilage damage by targeting hydrogel microsphere. Adv Mater 2024; 36: e2405943.

[18] Katsoula G, Lawrence JEG, Arruda AL, Tutino M, Balogh P, Southam L, Swift D, Behjati S, Teichmann SA, Wilkinson JM and Zeggini E. Primary cartilage transcriptional signatures reflect cell-type-specific molecular pathways underpinning osteoarthritis. Am J Hum Genet 2024; 111: 2735-2755.

[19] Kim JY, Rhim WK, Lee SY, Park JM, Song DH, Cha SG, Lee SH, Hwang DY, Kim BJ, Rho S, Ahn

TK, Park CG and Han DK. Hybrid nanoparticle engineered with transforming growth factor-β1-overexpressed extracellular vesicle and cartilage-targeted anti-inflammatory liposome for osteoarthritis. ACS Nano 2024; 18: 33937-33952.

[20] Liu N, Ma Y, Gong W, Shao X, Shi T, Li L, Wu W, Chen X, Shi Y, Zhang P, Lin J, Wang C, Fang D, Yang L, Wang P, Gao W, He Y, An X, Du R, Chen Y, Liu B, Qin J, Chen D, Cai P, Jiang Q and Guo B. Osteocyte-derived extracellular vesicles mediate the bone-to-cartilage crosstalk and promote osteoarthritis progression. Nat Commun 2025; 16: 4746.

[21] Mei H, Sha C, Lv Q, Liu H, Jiang L, Song Q, Zeng Y, Zhou J, Zheng Y, Zhong W, Zhou J and Li J. Multifunctional polymeric nanocapsules with enhanced cartilage penetration and retention for osteoarthritis treatment. J Control Release 2024; 374: 466-477.